

Vertical Phase Separation in Blended Organic Semiconducting Films and Impact on Their Electrical and Direct X-Ray Detection Properties

Maria Elisabetta Giglio, Elisabetta Colantoni, Ilaria Fratelli, Carme Martinez-Domingo, Pedro Martinez-Zaragoza, Giulia Napolitano, Enrico Campari, Paolo Branchini, Beatrice Fraboni, Laura Basiricó,* Luca Tortora,* and Marta Mas-Torrent*

Blends of small-molecule organic semiconductors (OSCs) and insulating polymers in Organic Field-Effect Transistors (OFETs) are mainly used to assist the solution-processing of OSCs, but they can also reduce interfacial charge traps due to vertical phase separation. Such charge traps are known to affect both the electrical response and radiation-induced charge collection capability in these devices. This study aims to optimize vertical phase separation in blend films of 1,4,8,11-tetramethyl-6,13-triethylsilylethynyl pentacene (TMTEs) and polystyrene (PS) to minimize charge trap density at the semiconductor/dielectric interface, thereby enhancing the electrical performance and direct X-ray detection sensitivity in OFETs. A PS mass concentration of 33% is identified as optimal for achieving high-quality phase separation and favorable film morphology. This formulation led to films with reduced interfacial hole trap density and improved electrical and detection capacity, demonstrating a hole field-effect mobility of $(1.3 \pm 0.4) \text{ cm}^2 \text{ V}^{-1} \text{ s}^{-1}$ and X-ray sensitivity of $(5.6 \pm 0.2) \times 10^3 \mu\text{C Gy}^{-1} \text{ cm}^{-2}$ at low applied voltages. Remarkably, the molecular weight of PS does not significantly impact vertical phase separation, thin film morphology, or electrical properties. These findings are crucial for the development of high-performance OFETs and their application as X-ray detectors.

are gaining considerable attention in applications where traditional inorganic materials fall short, such as in flexible displays, wearable sensors, and emerging technologies requiring adaptability.^[1–10] Compared to their inorganic counterparts, organic semiconductors (OSCs) offer distinct advantages such as reduced weight and compatibility with flexible substrates and economical large-area production methods.^[11–17] In particular, the use of solution shearing techniques to deposit the OSC active layers has emerged as a leading processing strategy for fabricating large-area devices at low cost and high throughput.^[18–24] These approaches can produce high-quality, crystalline organic films with precise control over molecular orientation and film structure.^[25–28]

To achieve high OFET performance, OSC films with high homogeneity, molecular order, and crystal packing – ensuring an efficient electronic overlap,

especially in the plane parallel to the conducting channel – are required.^[25,27,29–31] Additionally, the interfacial trap density plays a key role. In the energy gap of OSCs, electronic states can arise due to chemical impurities or defects that trap mobile

1. Introduction

Over recent years, there has been considerable progress in the advancements of Organic Field-Effect Transistors (OFETs), which

M. E. Giglio, C. Martinez-Domingo^[+], P. Martinez-Zaragoza, M. Mas-Torrent
Institute of Materials Science of Barcelona (ICMAB-CSIC)
Campus UAB, Bellaterra 08193, Spain
E-mail: mmas@icmab.es

 The ORCID identification number(s) for the author(s) of this article can be found under <https://doi.org/10.1002/aelm.202400887>

^[+]Present address: Institute of Microelectronics of Barcelona (IMB-CNM-CSIC), Campus UAB, Bellaterra 08193, Spain

© 2025 The Author(s). Advanced Electronic Materials published by Wiley-VCH GmbH. This is an open access article under the terms of the [Creative Commons Attribution](https://creativecommons.org/licenses/by/4.0/) License, which permits use, distribution and reproduction in any medium, provided the original work is properly cited.

DOI: 10.1002/aelm.202400887

E. Colantoni, P. Branchini, L. Tortora
National Institute for Nuclear Physics (INFN)
Section of Roma Tre
Via della Vasca Navale 84, Rome 00146, Italy
E-mail: luca.tortora@uniroma3.it

E. Colantoni, I. Fratelli, G. Napolitano, E. Campari, B. Fraboni, L. Basiricó
Department of Physics and Astronomy
University of Bologna
Viale C. Berti Pichat 6/2, Bologna 40127, Italy
E-mail: laura.basirico2@unibo.it

I. Fratelli, B. Fraboni, L. Basiricó
National Institute for Nuclear Physics (INFN)
Section of Bologna
Viale C. Berti Pichat 6/2, Bologna 40127, Italy
L. Tortora
Department of Sciences
University of Roma Tre
Via della Vasca Navale 84, Rome 00146, Italy

charge carriers, causing OFETs to deviate from ideal behavior.^[32] Charge traps can result in diminished OFET mobility, increased threshold voltage (V_{th}), increased subthreshold swing (SS), and hysteresis in electrical curves, among other issues. To minimize electronic traps, various strategies for passivating the OSC/dielectric interface have been developed, such as preparing self-assembled monolayers on the dielectric surface^[33–35] or using OSC blends.^[25,36–41] The presence of traps for majority carriers can also significantly impact OFET performance when used as photodetectors, due to the reduction in charge collection capability.^[42–44]

The development of OFETs for direct X-ray detection has recently garnered extensive attention.^[45–51] As noted earlier, OSCs provide advantages over traditional inorganic materials, making them well-suited for applications requiring portable and adaptable detection systems, such as medical imaging and security screening.^[52–57] Furthermore, OSCs have a low capacity for absorbing ionizing radiation due to their low atomic number and density, making their radiation absorption similar to that of human tissue. This unique feature makes OSCs highly promising for integration in medical dosimetry, as it eliminates the need for complex calibration procedures and enables the creation of a low-interference sensor that can be placed between the radiation source and the patient without perturbing the primary beam.^[45,58–61] While human tissue equivalence represents a highly desirable property for developing personal radiation dosimeters, it also presents a major challenge in achieving high X-ray detection capability with these materials. Besides the low absorption of OSCs at high radiation energy, it is worth mentioning that another great challenge for the development of large-area organic electronics is the reliability and reproducibility of the devices, especially for their scaling up to multipixel and large-area devices.

Previously, we reported the fabrication of OFETs for X-ray detection based on thin films of blends of p-type small molecule OSCs (i.e., 6,13-bis(triisopropylsilyl)ethynyl) pentacene (TIPS-pentacene), 1,4,8,11-tetramethyl-6,13-triethylsilyl ethynyl pentacene (TMTES) and polystyrene (PS) prepared using the Bar-Assisted Meniscus Shearing Technique (BAMS).^[17,62–64] This work demonstrated that the addition of PS significantly decreases the density of interfacial traps for majority carriers (holes). This effect was attributed to the vertical phase separation occurring during OSC deposition, which resulted in the passivation of the trap states at the dielectric/OSC interface. Consequently, this improved the electrical mobility of the device leading to an enhanced charge collection and X-ray sensitivity. Consequently, a record sensitivity of $(1.65 \pm 0.05) \times 10^5 \mu\text{C Gy}^{-1} \text{cm}^{-2}$ for X-ray detection was achieved.^[62]

Control over phase separation is crucial for preparing homogeneous films and enhancing device performance. Ideally, the OSC molecules should organize into a well-ordered layer at the dielectric interface, establishing a channel with high charge carrier mobility.^[65] Poor phase separation, however, can lead to a mixed phase at the active interface with disordered domains, resulting in reduced charge transport efficiency and lower mobility in OFET devices.^[66] Several factors can influence phase separation, such as the polymer binder's permittivity,^[40,67] the substrate surface energy,^[68,69] or the OSC formulation.^[70]

In this study, we aimed to systematically explore the influence of the (OSC):(Polymer) ratio and the polymer molecular weight on the thin films' morphological characteristics and assess their impact on the interfacial charge traps and the overall device's electrical and detecting performance. Specifically, we selected blend films of TMTES:PS as active OFET layers deposited via BAMS (Figure 1a,b), since these have previously shown outstanding performance and X-ray sensitivity.^[62] Our findings indicate that adding a PS mass percentage of 15% sufficiently minimizes the density of interfacial charge traps for majority charge carriers (i.e., holes), due to effective phase separation and dielectric passivation, as confirmed by Time-of-Flight Secondary Ion Mass Spectrometry (ToF-SIMS) measurements. However, the optimal outcome in electrical mobility and X-ray sensitivity was obtained with 33% PS, where films were morphologically more homogenous. These results provide insights into the role and control of phase separation and interfacial charge traps in enhancing OFET performance and allow for optimization of detector sensitivity to X-rays.

2. Results

OFETs in a bottom-gate, bottom-contact (BGBC) configuration using interdigitated gold source-drain electrodes on Si/SiO_x substrates were fabricated (Figure 1b). Thin films of TMTES, as well as TMTES blended with PS, were prepared as active layers using the BAMS technique at a deposition speed of 10 mm s⁻¹ under ambient conditions (see details in Experimental Section). Building on previous studies,^[62] we used PS as a low-permittivity binder polymer and prepared 2% w/w solutions of pristine TMTES and TMTES blended with PS (280 kDa) in chlorobenzene. Previously, we also tested other binding polymers such as poly(pentafluorostyrene) (PFS) and poly(methyl methacrylate) (PMMA); however, the use of PS consistently led to devices with higher performance and a lower level of interfacial charge traps, probably due to its apolar nature and the fact it does not interact strongly with the OSCs.^[41,42,71] Our goal here was to identify the optimal PS concentration required to achieve effective phase separation, as shown in Figure 1c (i.e., efficient dielectric/semiconductor trap passivation), and to preserve good crystallization of the OSC for maximizing device performance. For this, we tested a range of TMTES:PS volume ratios, expressed as PS percentages with respect to the total mass: 2.5%, 5%, 10%, 15%, 20%, 33%, and 67%. Additionally, we fabricated devices by blending the semiconductor with PS of different average molecular weights (M_w) of 280, 100 and 10 kDa at TMTES:PS ratios of 20%, 33%, and 67%.

The devices were electrically analyzed under ambient conditions. Figure 2 displays the transfer characteristics in the saturation regime, bias stress, and shelf stability measurements for two representative devices: pristine TMTES and TMTES with 33% PS (280 kDa) (see Supporting Information section for output characteristics, Figure S1, Supporting Information, and additional formulations, Figure S2, Supporting Information). As shown in Figure 2a, the pristine TMTES OFETs exhibit pronounced hysteresis that can result from charge trapping,^[72–76] and a threshold voltage notably shifted toward positive values, with operation beginning at very high positive gate-source voltages (V_{GS}). Such a high positive V_{th} is indicative of unintentional doping.

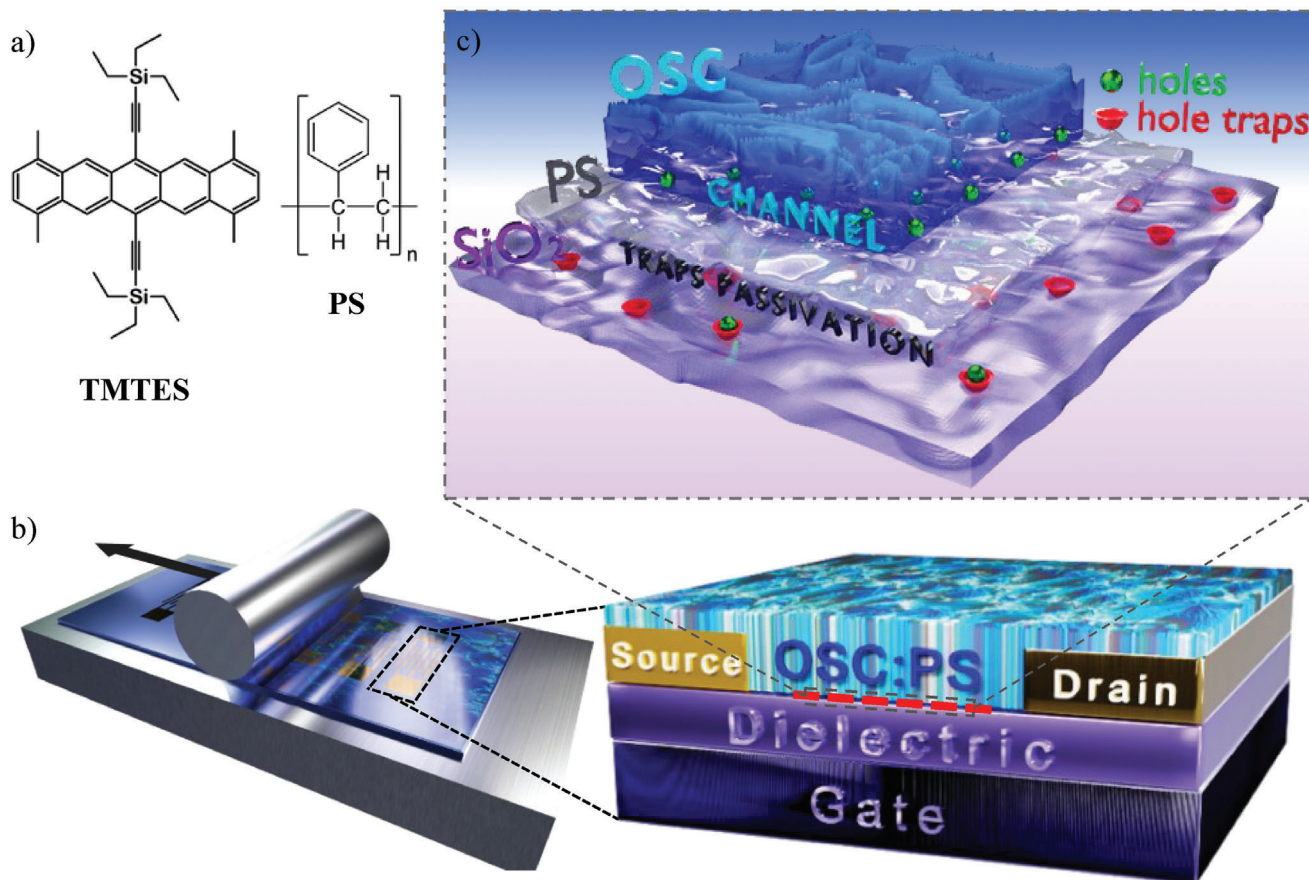


Figure 1. a) Molecular structures of the materials used in fabricating OFETs' active layer: the organic semiconductor TMTES and the polymer PS. b) On the left, a schematic of the BAMS technique, illustrates the formation of a crystalline OSC blended film. The steel bar moves unidirectionally (arrow direction), guiding the liquid meniscus over the substrate. On the right, the cross-sectional schematic of the OFETs fabricated in a BGBC configuration, underlying the charge traps at the SiO_x interface in dashed red c) Schematic illustration of vertical phase separation between TMTES and PS in the deposited film, resulting in the formation of a new OSC/PS interface on top of SiO_x dielectric layer.

In contrast, the TMTES:PS devices switch state within a much lower voltage window of 5 V and demonstrate superior electrical characteristics with minimal hysteresis and with a V_{th} close to 0 V (Figure 2d). This is an indication that the use of PS improves the stability and processability of the organic semiconductor under environmental exposure and also passivates charge carrier traps at the SiO_x interface. The incorporation of a less polar, low-dielectric constant polymeric layer on the dielectric should reduce dipolar disorder and minimize carrier localization at the interface, leading to a lowering of the charge trap density and a narrower density of trap states.^[38,41,64,77]

The operation stability of the TMTES OFETs with varying PS content was assessed through bias stress measurements conducted at a constant V_{GS} of -10 V and drain-source voltage (V_{DS}) of -1 V under ambient conditions between successive transfer curves. Bias stress characteristics are presented in Figure 2b,e, and Figure S2 (Supporting Information), with the extracted threshold voltage shifts over time shown in Figure S3 (Supporting Information). Pristine TMTES OFETs (0% PS) display a large positive V_{th} shift under bias stress, with an increase exceeding 10% from the initial value at 105 min which further rises to nearly 30% after 225 min (Figure 2b). Devices with low PS

content (2.5% and 5%) show moderate improvement in bias stability compared to pristine devices, with V_{th} shifts initially close to zero but gradually increasing with stress time. After 225 min, devices with 2.5% and 5% PS exhibit a shift of $\approx 12\%$, which reaches 20% at 285 min, indicating partial stabilization. At 10% PS content, a distinct shift behavior emerges, as devices begin exhibiting a negative threshold voltage shift instead of the positive trend seen in devices with lower PS content or no PS. This negative shift intensifies over time, reaching $\approx -20\%$ at 285 min. Devices containing 15% or higher PS content exhibit markedly enhanced bias stability, with threshold voltage shifts remaining below 10% up to 165 min and only reaching $\approx 12\%$ after 285 min, indicating a significantly stable performance over prolonged stress. As PS content increases further to 20% and 33% (Figure 2e), stability is enhanced even more, with V_{th} shifts remaining close to zero or slightly negative throughout the bias stress period. Notably, 15% PS can be identified as the minimum concentration required to achieve a notable reduction in bias stress shifts, likely due to effective trap passivation at the dielectric/semiconductor interface.

Our observations suggest that PS is influencing the charge dynamics at the semiconductor/dielectric interface, especially under prolonged bias stress.^[78,79] The positive V_{th} shifts observed

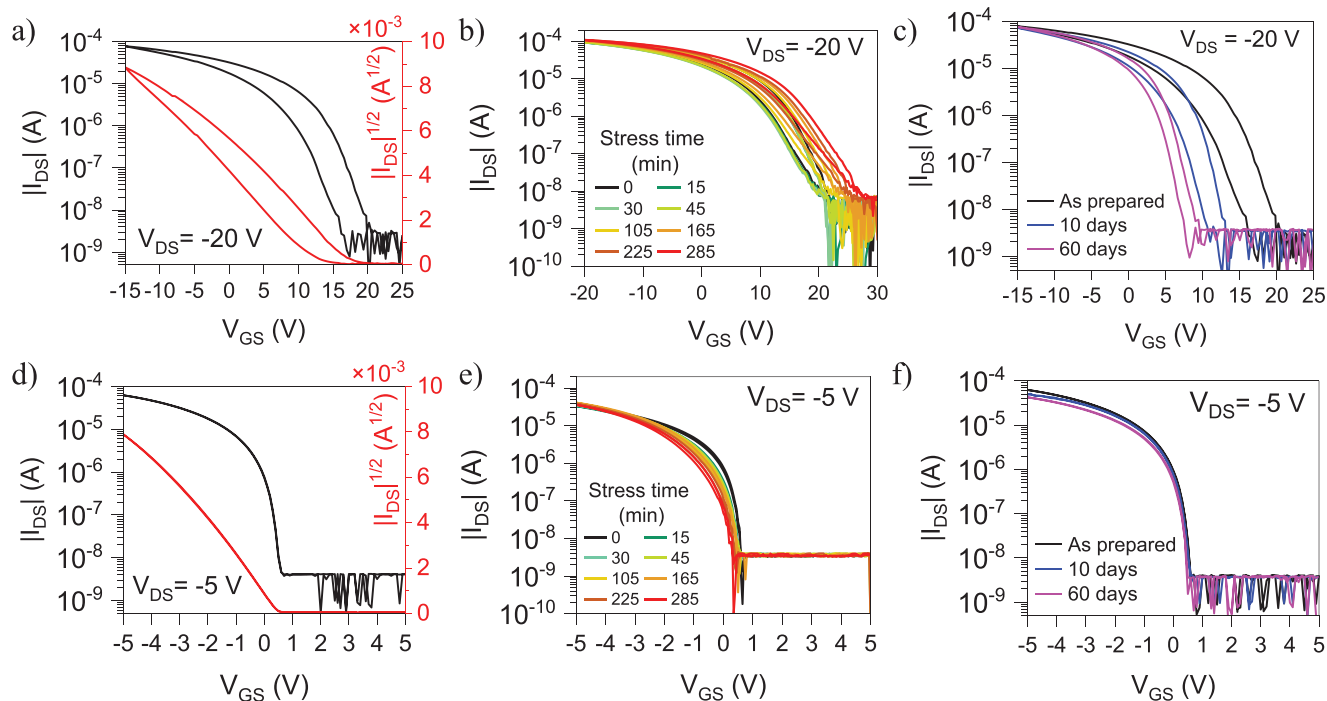


Figure 2. Electrical performance of two representative OFETs: a–c) pristine TMTES film and d–f) TMTES blended film with a 2:1 ratio (33% PS 280 kDa content). Panels a) and d) show the transfer characteristics in the saturation regime, b) and e) display the transfer curves after multiple cycles of bias stress at $V_{GS} = -10$ V and $V_{DS} = -1$ V, and c) and f) illustrate the shelf stability of the devices.

in devices with PS content <10% during the bias stress measurements performed under an ambient environment can be linked to doping effects from oxygen^[36,80,81] or to trapping of minority carriers (electrons) which lead to the injection of more mobile majority carriers (holes) to ensure charge neutrality.^[81–83] In the latter case, high gate voltages and prolonged stress would exacerbate electron injection and trapping, shifting the turn-on voltage for hole conduction to more positive values. In contrast, in the films with a PS content $\geq 10\%$ the negative V_{th} shift observed, commonly reported in the literature,^[32,84–88] is attributed to hole trapping near the semiconductor/dielectric interface. Traps often arise from OH groups, defects, and dipole moments on the SiO_2 surface, aggravated by water infiltration under applied gate and drain bias. Increasing the PS content further enhances the passivation of the hole traps at the SiO_2 interface, progressively stabilizing the device's performance under bias-stress conditions. Hence, the PS matrix prevents the formation of charge-trapping sites at the OSC/PS interface and inhibits the diffusion of oxygen and moisture into the OSC/dielectric interface.^[36]

Additionally, the TMTES:PS devices demonstrated excellent shelf stability, maintaining their operation unchanged for up to 60 days post-fabrication (Figure 2f). Conversely, the pristine TMTES OFETs show poor long-term stability, marked by a substantial negative shift in V_{th} over the same time period after fabrication, likely due to the progressive increase in water-induced traps due to prolonged storage of the devices and their exposition to air. (Figure 2c).^[89–91] This shift reached 57% with respect to the initial value measured on the preparation day.

The main electrical OFET parameters – hole field-effect mobility in saturation regime (μ_{sat}) and V_{th} – together with the interfa-

cial charge trap density estimated from the sub-threshold swing (see Experimental Section), have been extracted for all the devices and are illustrated in Figure 3 (data also summarized in Table S1, Supporting Information). It can be observed that devices based on pristine TMTES exhibit the lowest mobility and the highest positive threshold voltage. As the PS concentration increases, the device mobility improves (Figure 3a), and the V_{th} shifts toward 0 V (Figure 3b). At 15% of PS, the V_{th} stabilizes at a value close to 0 V, while the mobility keeps increasing until reaching its maximum value at 33% of PS. Beyond this point, adding more PS results in a mobility decrease. The maximum field-effect mobility achieved in saturation regime is $(1.3 \pm 0.4) \text{ cm}^2 \text{ V}^{-1} \text{ s}^{-1}$, more than an order of magnitude higher with respect to the pristine films which is $(0.09 \pm 0.01) \text{ cm}^2 \text{ V}^{-1} \text{ s}^{-1}$.

Analyzing the density of interfacial hole traps (N_t , Figure 3c), we observed the same trend as for the threshold voltage: N_t decreases with PS until stabilizing at 15% PS, where the trap density is almost one order of magnitude lower than the values found for the pristine films. Thus, this data suggests that 15% PS is the minimum required polymer amount to efficiently passivate traps at the dielectric/semiconductor interface, resulting in a lower density of hole traps and undoped devices. However, the charge transport along the OSC thin film is further improved by adding up to 33% of PS. This implies that, in addition to charge traps at the dielectric/semiconductor interface, other morphological factors may play a role in the thin film transport properties.

As previously mentioned, the OFETs were also characterized as X-ray detectors. In Figure 3d the OFETs sensitivity measured under X-ray exposure is reported. The devices were irradiated using X-ray radiation produced by a W-target X-ray tube kept

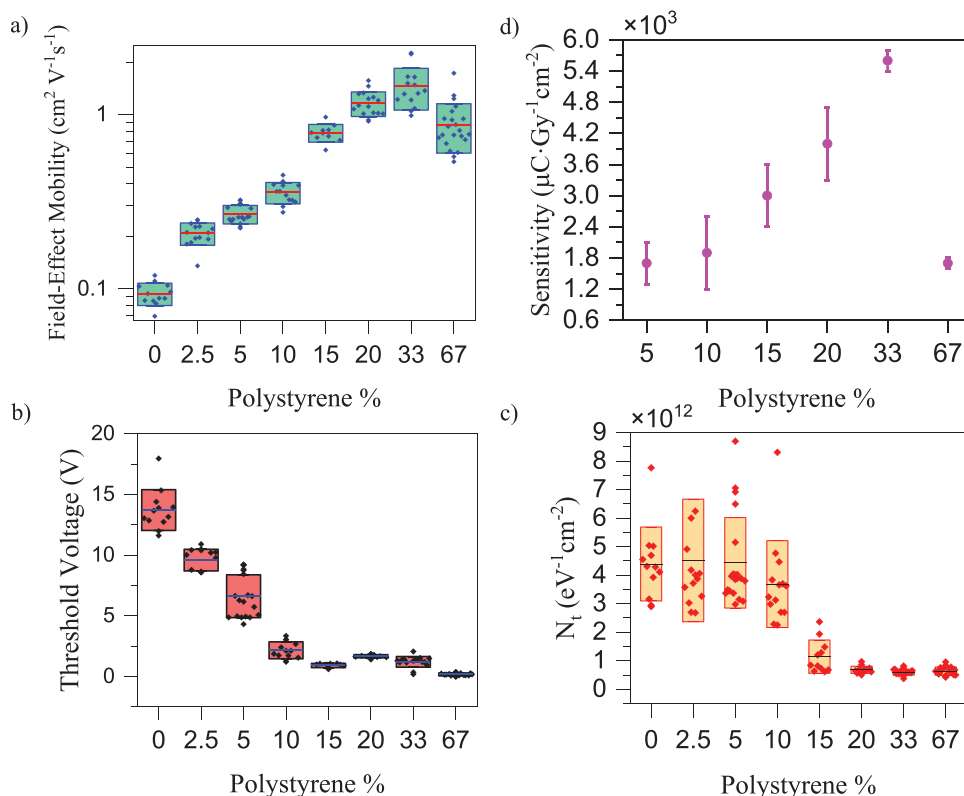


Figure 3. Mean values and standard deviations of key OFET parameters: a) hole field-effect mobility in the saturation regime, b) threshold voltage, c) density of hole traps at the dielectric interface, and d) sensitivity in X-ray detection. Measurements were conducted for active layers consisting of pristine TMTES and TMTES blends at various TMTES:PS blending ratios, expressed as PS (280 kDa) mass percentages.

at 40 kVp and by varying the intensity of the beam in the dose rate range of 1.3 – 6.6 mGy s⁻¹. During the experiment, the radiation-induced photocurrent flowing within the OFET channel was monitored in real-time by externally biasing the device in a saturation regime ($V_{GS} = -2.5$ V and $V_{DS} = -10$ V). The detector was subjected to initial conditioning (i.e., biasing in the dark condition) for 2 min in order to reach the dynamic equilibrium of the system and reduce bias stress effects to negligible values. The sensitivity values have been extracted from the Photocurrent versus Dose Rate plots as the slope of the linear fitting curve (see Experimental Section and Figure S4, Supporting Information). The X-ray sensitivity trend with PS concentration shown in Figure 3d (see also Table S1, Supporting Information) follows the same behavior as the OFET mobility, reaching the highest value at a PS mass percentage of 33%, where a sensitivity of $(5.6 \pm 0.2) \times 10^3 \mu\text{C Gy}^{-1} \text{cm}^{-2}$ was measured, which is consistent with our previous findings.^[62] The similar trend observed for electrical mobility and X-ray sensitivity demonstrates that the optimization of the OFET transport properties (i.e., passivation of trap states for majority carriers and fine-tuning of the OSC crystallization process) is an effective route to boost the collection efficiency of the detector.

To confirm that the observed variations in device performance are exclusively attributable to changes in crystal domain size and phase separation effectiveness and not to the formation of different polymorphs, we performed X-ray diffraction (XRD) analysis on all deposited films (Figure S5, Supporting Information).

As described in our previous study,^[62] the XRD measurements showed only peaks corresponding to crystals oriented with the *ab* plane parallel to the substrate. Additionally, all films crystallize in the Polymorph II (PII) phase, which is known for its herringbone stacking motif.^[92]

The films' morphology was characterized using Cross-Polarized Optical Microscopy (POM), Atomic Force Microscopy (AFM), and surface chemical mapping through ToF-SIMS. Additionally, chemical depth profiling analysis was performed using ToF-SIMS to evaluate the phase separation between the OSC and the binder polymer, following the experimental approach already adopted in previous works.^[62,93,94]

POM images of the films with 0%, 15%, 33%, and 67% PS content are shown in Figure 4a (see Figure S6a, Supporting Information for additional formulations). The images show the formation of highly crystalline films with extensive coverage and morphological uniformity, exhibiting spherulitic domains. A significant change in the density of crystal domains between the pristine and blended films can be also observed, as confirmed by the ToF-SIMS surface chemical maps of total ions shown in Figure 4b. Both POM and ToF-SIMS techniques reveal that as the PS content increases, the films become increasingly homogeneous, with this trend continuing up to 33% PS. Beyond this concentration, however, film uniformity decreases. This finding is in accordance with the mobility and sensitivity trend that we discussed above.

In order to gain insights into the vertical phase separation, ToF-SIMS depth profiles of TMTES, PS, and SiO₂ were determined

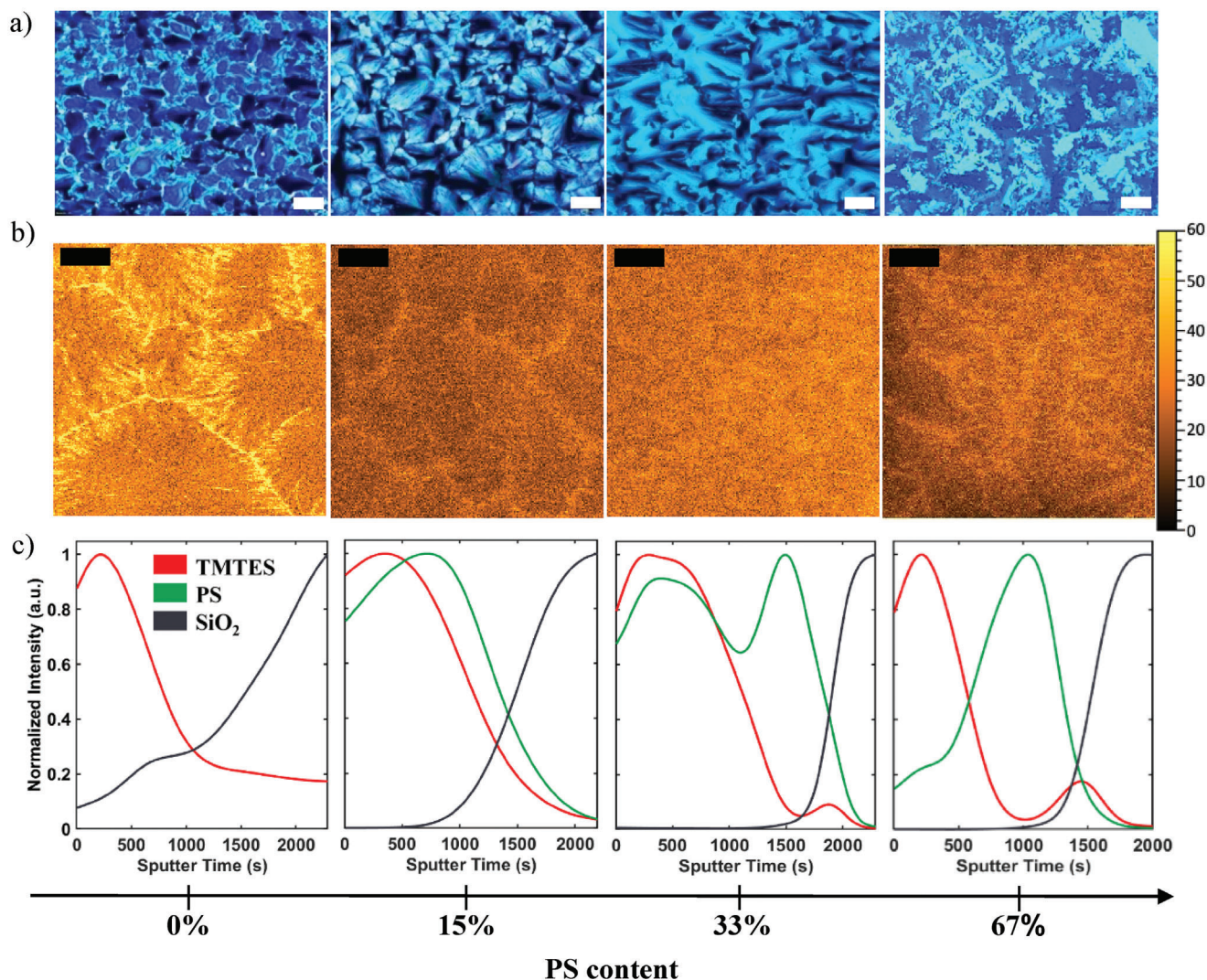


Figure 4. a) POM images with a 50 μm scale bar (white). b) ToF-SIMS surface chemical maps of total ions with a 20 μm scale bar (black). c) Normalized (to maximum) depth profiles obtained by ToF-SIMS in the channel area of the OFETs. The PS (280 kDa) content in the film increases progressively from left to right as a percentage of the total mass (TMTES + PS). The ToF-SIMS analysis starts at the film's outer surface and extends to the SiO₂ layer. The TMTES signal is represented by average of SiC⁻, SiCH⁻, SiC₂H⁻, SiC₅H₂⁻, SiC₇H₂⁻ species (red curve), the PS signal by the average C₃H₃⁻, C₄H₃⁻, C₅H₃⁻, C₆H₃⁻, C₇H₃⁻ ions (green curve), and substrate is represented by the SiO₂⁻ ion (black curve).

by averaging the intensities of their characteristic secondary ions (Figure 4c; Figure S6b,c, Supporting Information). Specifically, for TMTES the average signal was obtained using SiC⁻, SiCH⁻, SiC₂H⁻, SiC₅H₂⁻, SiC₇H₂⁻ species, and C₃H₃⁻, C₄H₃⁻, C₅H₃⁻, C₆H₃⁻, C₇H₃⁻ ions for PS. SiO₂⁻ ion was selected as a tracking signal or the substrate. Detailed methodology for this analysis can be found in the Experimental Section. These ions originate from the active channel region of the OFETs and the dielectric surface. In the sample without PS, the characteristic signal of TMTES (red curve) shows a well-defined OSC layer. When the PS is added at a low percentage (2.5%, 5%, 10%), the semiconductor layer seems to be well mixed with the polymer; this can be appreciated in Figure S6 (Supporting Information) where the PS signal (green curve) reveals a depth distribution similar to TMTES. At 15% PS (Figure 4c), the localization of the polymer starts to change, indicating a segregation of PS from the TMTES. This transition re-

gion becomes more pronounced at 33% and 67% PS, suggesting that when the polymer concentration becomes prevalent with respect to the OSC, a vertical phase separation occurs between the two compounds.

These results further confirm that PS acts as an effective dielectric passivation layer. They also establish a threshold of 15% PS content, from which point the vertical phase separation between the OSC and the polymer becomes evident. These findings are in agreement with the electrical characterization, since at this PS content the density of hole traps and the threshold voltage reach the optimum values. Moreover, the amount and size of the crystal domains (Figure 4a; Figure S6a, Supporting Information) continue to change with increasing PS concentration up to 33%, which is the formulation where the highest field-effect mobility and X-ray sensitivity were found. Consequently, variations in mobility and X-ray sensitivity in the range 15–33% PS

are more closely associated with changes in thin film morphology (i.e., grain density in the crystal domains), rather than with interfacial trap states passivation which is already optimized with a 15% PS content. The observed variations in domain size are likely attributed to the increased vertical phase separation as the presence of PS is enhanced. We cannot rule out that the use of another coating technique or the modification of the deposition parameters, such as temperature or speed, could permit us to further increase the percentage of PS above 33% without compromising the thin film homogeneity and the device performance. However, this is out of the scope of this work.

Further characterization of the TMTES and TMTES:PS thin films was performed using AFM, as shown in Figures S7 and S8 (Supporting Information). The films demonstrated notably low surface roughness, with mean values of 25.1 ± 0.9 nm for pristine TMTES and down to 5.3 ± 0.4 nm for TMTES at 33% PS content. Roughness values for all PS percentages and molecular weights are detailed in Figure S8a (Supporting Information). Additionally, the average thickness of the pristine and blended films was measured to be 34 ± 1 and 42 ± 2 nm, respectively, as shown in Figure S8b (Supporting Information). As expected, increasing the PS content results in progressively smoother and more homogeneous film surfaces. The presence of PS in solution enhances surface wettability, promoting better spreading and leveling of the OSC layer while also supporting the crystallization process of the OSC.^[22,38,95–105] Furthermore, optimized PS content and effective phase separation mitigate the roughness typically associated with large grains and grain boundaries, yielding well-defined domains, improved molecular alignment, and fewer defects.^[40,66,67,106–109]

We further investigated the effect of blending PS with lower M_w (i.e., 10 and 100 kDa), maintaining a constant PS content of 33%. Surprisingly, our analysis showed minimal impact of PS molecular weight on phase separation, crystallization, electrical performance, or X-ray sensitivity (Figure 5). The key electrical parameters for different M_w are presented in Figure 5a,b, and Table S1 (Supporting Information). Electrical characteristics and AFM topological images are reported in Figures S9 and S10 (Supporting Information), respectively.

Previous studies have demonstrated that varying the M_w of binder polymers like PS significantly influences viscosity, solubility, miscibility, and phase separation, which in turn affect film morphology and charge transport.^[27,38,100,105,110–112] In addition, factors such as solvent choice, surface energy, coating technique, and coating parameters play essential roles in regulating phase segregation and the compositional structure of blend films. A previous work on TIPS-pentacene blends with PS highlighted the dependence of the polymer M_w on the device performance.^[101] It was found that there was an interplay between the coating speed and M_w that determined the device mobility. Interestingly, it was found that at the highest tested shearing speed (4 mm s^{-1}), mobility was largely unaffected by M_w . Similarly, a study on the OSC DiF-TES-ADT blended with PS showed that increasing solution shearing speed from 0.1 to 1.7 mm s^{-1} reduced mobility differences across a broad range of PS M_w (from 10^4 to 10^6).^[99] The authors also reported that the use of high- M_w led to films with larger crystalline domains and more efficient phase separation, which was attributed to the higher solution viscosities of high- M_w solutions that promoted more homogeneous films. In

all these examples, the deposition rate is very low, so it is expected that in the coating process, a wet film is first formed and then the OSC crystallizes. In our work, the TMTES:PS films are deposited at a much higher solution shearing speed of 10 mm s^{-1} . In this regime, the crystallization occurs in the evaporation regime and the OSC crystallizes in the meniscus line during the coating. Thus, evaporation dynamics appears to be the dominant factor affecting the thin film morphology and phase separation, and ultimately the electrical properties of the devices. In our particular case, we observed no significant impact on phase separation, trap passivation, and film homogeneity with varying PS M_w , leading to similar transport properties across all M_w tested. Although a few studies have explored systematically the effect of PS M_w on phase separation and charge transport in OFETs, our results align with previous findings, suggesting that at high shearing speeds when the OSC crystallization is faster, both morphology and phase separation are less affected by M_w . Thus, our results indicate that in our system and with the tested M_w range, adjusting the concentration of PS is more critical for achieving enhanced performance than varying its molecular weight.

3. Conclusion

This work shows that adding PS, an insulating polymer with low permittivity, significantly improves the processability, crystallinity, electrical response, and stability of TMTES-based OFETs. The devices also exhibited enhanced sensitivity under X-ray exposure, emphasizing their potential for applications in X-ray detection.

Our results show that PS concentration plays a crucial role in determining device operation. We explored various TMTES:PS ratios (as PS mass content %) to identify the ideal concentration for achieving effective phase separation and maximum performance. A PS content of 15% and above consistently promoted appropriate phase segregation to achieve efficient interface passivation. This leads to devices with a minimized density of interfacial traps exhibiting a higher environmental and operational stability. However, thin film uniformity can be further optimized, which can be caused by an enhanced vertical phase separation, by increasing the PS content up to 33%, where the maximum field-effect mobility and X-ray sensitivity are observed. However, beyond this concentration, crystallization quality begins to deteriorate, leading to reduced mobility and X-ray sensitivity. Additionally, the average molecular weight of PS was found to have no significant impact on crystallization, electrical properties, or sensitivity to X-rays, suggesting that optimizing PS concentration is more critical than its molecular weight in the coating conditions used in this study. Remarkably, the optimized devices found with a 33% PS exhibited a high hole field-effect mobility of $(1.3 \pm 0.4) \text{ cm}^2 \text{ V}^{-1} \text{ s}^{-1}$ and X-ray sensitivity of $(5.6 \pm 0.2) \times 10^3 \text{ } \mu\text{C Gy}^{-1} \text{ cm}^{-2}$ at low operating voltages ($V_{GS} = -2.5 \text{ V}$ and $V_{DS} = -10 \text{ V}$).

This study demonstrates that the use of binding polymers represents a highly promising route to realize reliable OFETs, which can be fabricated using a scalable low-cost printing technique. Further, this work sheds light on the key factors that influence their performance, reliability, and also their X-ray detection capabilities, laying the groundwork for practical applications in direct high-energy radiation sensing with organic materials, such as for medical dosimetry and diagnostic purposes.

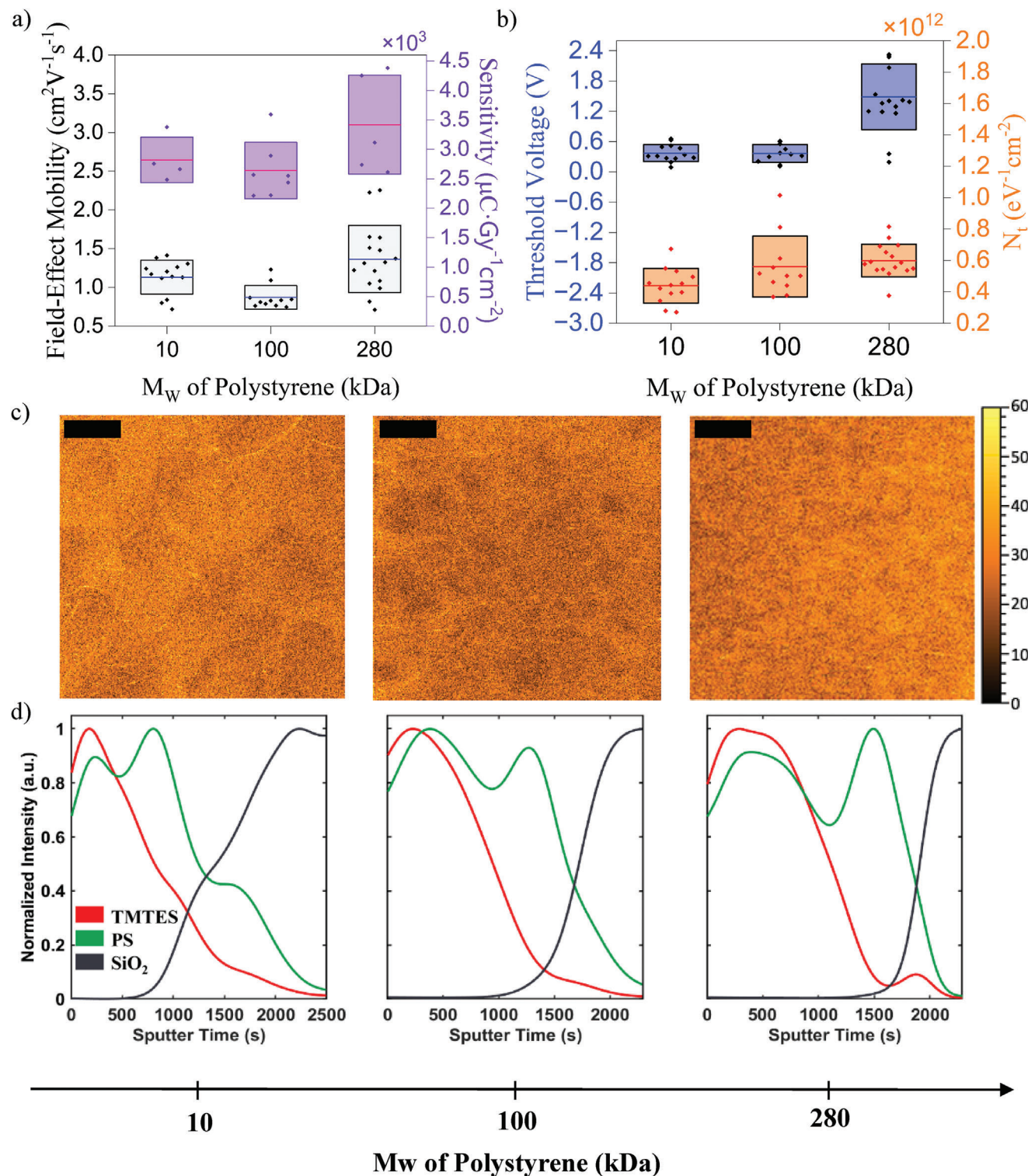


Figure 5. a) Hole field-effect mobility and X-ray detection sensitivity. b) Threshold voltage and charge trap density for majority carriers (holes) at the dielectric interface. These values were obtained from OFETs with TMTES films blended with 33% PS content, using different PS M_w . c) ToF-SIMS surface chemical maps of total ions with a 20 μm scale bar (black). d) Normalized (to maximum) depth profiles obtained by ToF-SIMS in the OFET channel area. Here, the molecular weight of PS (33% content) increases from left to right. The ToF-SIMS analysis spans from the film's outer surface to the SiO_2 layer. The TMTES signal is represented by the average of SiC^- , SiCH^- , SiC_2H_2^- , SiC_5H_2^- , SiC_7H_2^- species (red curve); the PS signal by the average C_3H_3^- , C_4H_3^- , C_5H_3^- , C_6H_3^- , C_7H_3^- ions (green curve); the substrate is represented by the SiO_2^- ion (black curve).

4. Experimental Section

Materials and Solutions Preparation: TMTES and PS with molecular weights of 10, 100, and 280 kDa were sourced from Ossila and Merck, respectively, and used as received. 2,3,4,5,6-pentafluorothiophenol (PFBT) was purchased from Merck. Solutions of TMTES and PS were separately prepared in anhydrous chlorobenzene with a concentration of 2.0% w/w. For the preparation of blends, these solutions were mixed in TMTES:PS volume ratios of 39:1, 19:1, 9:1, 17:3, 4:1, 2:1, and 1:2, yielding final PS concentrations of 2.5%, 5%, 10%, 15%, 20%, 33%, and 67% by mass. The solutions were fully dissolved at 60 °C and heated to 105 °C, the deposition temperature, immediately before use.

Device Fabrication: Interdigitated gold electrodes were patterned on heavily p-doped silicon wafers (Si-Mat) with a 200 nm SiO₂ layer using positive photolithography. A 5 nm chromium adhesion layer followed by a 40 nm gold layer was thermally evaporated onto the wafers. The device geometry was designed with a channel length (L) of 25 μm and a width/length (W/L) ratio of 100, resulting in a pixel area of 3.825 × 10⁻³ cm². Substrates underwent a cleaning procedure involving three 15-minute sonication cycles in acetone, followed by isopropanol (HPLC grade), and were dried using a nitrogen flow.

The gold surfaces of the electrodes were exposed to ultraviolet ozone treatment for 25 min and then immersed in a 15 mM solution of 2,3,4,5,6-pentafluorothiophenol (PFBT) in isopropanol for 15 min to form a self-assembled monolayer. The substrates were subsequently rinsed with pure isopropanol to remove excess PFBT and dried under nitrogen.

The deposition of the active semiconductor layer was performed using the Bar-Assisted Meniscus Shearing (BAMS) technique, a method selected for its precision in controlling film thickness and morphology. The TMTES solutions, prepared as described, were utilized as inks for this process. To initiate the thin-film coating, substrates were placed on a heated platform maintained at 105 °C. A volume of ≈40 μL of the blend solution was dispensed between the substrate and a cylindrical steel bar designed for the BAMS method. The meniscus was then sheared across the substrate at a controlled speed of 10 mm s⁻¹. This shearing action facilitated uniform film formation, while the elevated temperature promoted rapid solvent evaporation, resulting in immediate film drying.

All deposition and coating steps were carried out under ambient conditions, which ensured consistent film quality without necessitating additional post-deposition thermal treatments.

Film Characterization: Optical microscopy was performed using an Olympus BX51 microscope equipped with a polarizer and analyzer to capture detailed images of the thin films. The images were taken under bright field and cross-polarization conditions using two polarizer filters at 5×, 20× and 50× magnification.

XRD was conducted using a Siemens D5000 diffractometer, employing Cu K-alpha radiation with a wavelength of 0.1540560 nm in a theta/2theta geometry to analyze the crystalline structure of the films.

AFM imaging was carried out with a Park System NX10. AFM measurements were conducted in non-contact mode. The resulting topographical data were analyzed using Gwyddion software, where a specific tool within the software was employed to calculate the roughness and thickness of the films.

ToF-SIMS measurements were performed using a ToF-SIMS V instrument (ION-TOF GmbH, Muenster, Germany). A low-energy electron flood gun (20 V) was used for charge compensation. The base pressure of the analysis chamber during the ToF-SIMS data acquisition was equal to 10–9 mbar. Surface analysis data were acquired in high lateral resolution mode using Bi³⁺⁺ primary ions at 30 keV with a pulse width of 18.4 ns and a current emission of 0.4 pA. For depth profiling in dual-beam mode, the analysis beam was combined with a sputter ion gun producing Cs⁺ ions at 500 eV (current 10 nA). The analysis area of the surface chemical maps was 100 μm × 100 μm. Sputtering was carried out over 300 μm × 300 μm areas inside the OFET active layer. Depth profiles were acquired over 100 μm × 100 μm areas within the center of the sputter crater. Secondary ions were extracted at 2 kV and detected with a time-of-flight mass analyzer. A cycle time of 100 μs allowed to obtain a mass range from 1 to 900 m/z. Negative mass spectra were calibrated using CH⁻, Si⁻, C₅⁻, and C₄₂H₅₀Si₂⁻

signal peaks. The mass resolution achieved was more than 5000 m/Δm for all the analyzed masses. Mass spectra and depth profile signals were exported for further analysis by SurfaceLab v6.5 software. A list of characteristic secondary ions was obtained for TMTES and PS mass spectra through a multivariate analysis approach.

Device Characterization: The OFETs were analyzed by measuring their transfer and output characteristics using an Agilent B1500A semiconductor device analyzer connected to a Karl SÜSS probe station, all conducted under ambient conditions without encapsulation of the devices. The hole field-effect mobility and the threshold voltage were determined in the saturation regime. Mobility was calculated following Shockley's classic FET model and is described by the following equation:

$$\mu_{sat} = \frac{2L}{WC_{ox}} \left(\frac{\partial \sqrt{|I_{DS}|}}{\partial V_{GS}} \right)^2 \quad (1)$$

where C_{ox} is the insulator capacitance per unit area (17.26 nF cm⁻²), and W and L are the channel width and length, respectively. A linear fit of the square root of the measured drain-source current (I_{DS}) versus V_{GS} was applied to derive μ_{sat} and V_{th}. The subthreshold swing was calculated and used to estimate the density of interfacial traps for majority carriers (holes) per unit area.^[113]

$$SS = \left(\frac{\partial (\text{Log}|I_{DS}|)}{\partial V_{GS}} \right)^{-1} \quad (2)$$

$$N_t \approx \frac{C_{ox}}{q} \left[\frac{qSS}{k_B T \ln(10)} - 1 \right] \quad (3)$$

where q is the electronic charge, k_B is the Boltzmann constant, and T is the absolute temperature. Device parameters were extracted from 135 devices to ensure consistency and reproducibility.

Bias stress measurements of the OFETs were conducted at constant V_{GS} of -10 V and V_{DS} of -1 V, under ambient conditions, between successive transfer characteristic measurements. Shelf stability was assessed by storing the samples in an inert atmosphere and measuring their transfer characteristics in saturation regime under ambient conditions.

For X-ray irradiation tests, the X-ray broad spectrum provided by a tungsten-target tube with an accelerating voltage of 40 kVp and dose rates in the range 1.3–6.6 mGy s⁻¹, measured with an error below 5% by means of the BARRACUDA X-Ray Analyser from RTI was employed. The mean photon energy in this irradiation condition was 15.2 keV. During these measurements, the samples were kept in a metal Faraday cage to keep the sample in the dark and to screen the external electromagnetic noise. The devices were irradiated by four subsequent 60 s irradiation cycles followed by 60 s of X-ray off. During the experiment the OFETs were biased (V_{GS} = -2.5 V and V_{DS} = -10 V) and the current flowing in the OFET's channel I_{DS} was continuously monitored in real-time. The detector was subjected to an initial conditioning (i.e., biasing in the dark condition) for 2 min. The photocurrent induced for each X-ray beam intensity was calculated as the difference between the I_{DS} when the sample was irradiated and the I_{DS} flowing in the dark condition. The sensitivity was calculated as the linear fitting curve slope of the Photocurrent versus Dose Rate plot.

Supporting Information

Supporting Information is available from the Wiley Online Library or from the author.

Acknowledgements

M.E.G., E.C., and I.F. contributed equally to this work. This work was funded by Ministerio de Ciencia e Innovación

MCIN/AEI/10.13039/501100011033/ERDF, UE with project SENSATION PID2022-141393OB-I00, and through the “Severo Ochoa” Programme for Centers of Excellence in R&D (CEX2023-001263-S) and the Generalitat de Catalunya (2021-SGR-00443). M.E. acknowledges her FPI fellowship and is enrolled in the UAB Materials Science PhD program. L.B. and G.N. acknowledge the RELOAD project funded by Fondazione Cariplo and Fondazione CDP, Grant No. 2022–1834. I.F. received funding from the European Union’s Horizon Europe research and innovation program under the Marie Skłodowska-Curie Actions grant agreement No 101105245. The Grant of Excellence Departments 2023–2027, MIUR (ARTICOLO 1, COMMI 314–337 LEGGE 232/2016), is gratefully acknowledged by L.T. The authors acknowledge support of the publication fee by the CSIC Open Access Publication Support Initiative through its Unit of Information Resources for Research (URICI).

Conflict of Interest

The authors declare no conflict of interest.

Data Availability Statement

The data that support the findings of this study are available from the corresponding author upon reasonable request.

Keywords

organic field-effect transistors, organic semiconductor blends, solution shearing, vertical phase separation, X-rays detectors

Received: November 23, 2024

Revised: February 3, 2025

Published online:

- [1] P. C. Y. Chow, T. Someya, *Adv. Mater.* **2020**, *32*, 1902045.
 [2] B. King, B. H. Lessard, *J. Mater. Chem. C* **2024**, *12*, 5654.
 [3] G. Lee, Q. Wei, Y. Zhu, *Adv. Funct. Mater.* **2021**, *31*, 2106475.
 [4] X. Liu, H. Li, M. Tao, Y. Yu, Z. Zhu, D. Wu, X. Hu, Y. Chen, *Adv. Mater. Technol.* **2024**, *10*, 2400661.
 [5] S. Nasiri, M. R. Khosravani, *Sens. Actuators, A* **2020**, *312*, 112105.
 [6] J. Song, H. Liu, Z. Zhao, P. Lin, F. Yan, *Adv. Mater.* **2024**, *36*, 2300034.
 [7] Y. Weng, Z. Yu, T. Wu, L. Liang, S. Liu, *New J. Chem.* **2023**, *47*, 5086.
 [8] “35 years of organic transistors | Nature Electronics,” can be found under <https://www.nature.com/articles/s41928-021-00642-5>, **2024**.
 [9] H. Siringhaus, *Adv. Mater.* **2014**, *26*, 1319.
 [10] K. Liu, B. Ouyang, X. Guo, Y. Guo, Y. Liu, *npj Flex Electron* **2022**, *6*, 1.
 [11] S. Morab, M. M. Sundaram, A. Pivrikas, *Coatings* **2023**, *13*, 1657.
 [12] A. K. Chauhan, P. Jha, D. K. Aswal, J. V. Yakhmi, *J. Electron. Mater.* **2022**, *51*, 447.
 [13] Y. Zhao, W. Wang, Z. He, B. Peng, C.-A. Di, H. Li, *Chin. Chem. Lett.* **2023**, *34*, 108094.
 [14] R. K. Cavin, P. Lugli, V. V. Zhirnov, *Proc. IEEE* **2012**, *100*, 1720.
 [15] C. S. Buga, J. C. Viana, *Adv. Mater. Technol.* **2021**, *6*, 2001016.
 [16] J. Wiklund, A. Karakoç, T. Palko, H. Yiğitler, K. Ruttik, R. Jäntti, J. Paltakari, *J. Manuf. Mater. Process.* **2021**, *5*, 89.
 [17] S. Chen, Z. Li, Y. Qiao, Y. Song, *J. Mater. Chem. C* **2021**, *9*, 1126.
 [18] A. C. Arias, J. D. MacKenzie, I. McCulloch, J. Rivnay, A. Salleo, *Chem. Rev.* **2010**, *110*, 3.
 [19] C. d. Dimitrakopoulos, P. r. I. Malenfant, *Adv. Mater.* **2002**, *14*, 99.
 [20] R. Abbel, Y. Galagan, P. Groen, *Adv. Eng. Mater.* **2018**, *20*, 1701190.
 [21] L. Basiricò, G. Mattana, M. Mas-Torrent, *Front. Phys.* **2022**, *10*, <https://doi.org/10.3389/fphy.2022.888155>.
 [22] I. Temiño, F. G. Del Pozo, M. R. Ajayakumar, S. Galindo, J. Puigdollers, M. Mas-Torrent, *Adv. Mater. Technol.* **2016**, *1*, 1600090.
 [23] F. G. del Pozo, S. Fabiano, R. Pfattner, S. Georgakopoulos, S. Galindo, X. Liu, S. Braun, M. Fahlman, J. Veciana, C. Rovira, X. Crispin, M. Berggren, M. Mas-Torrent, *Adv. Funct. Mater.* **2016**, *26*, 2379.
 [24] A. Tavasli, B. Gurunlu, D. Gunturkun, R. Isci, S. Faraji, *Electronics* **2022**, *11*, 316.
 [25] S. Galindo, A. Tamayo, F. Leonardi, M. Mas-Torrent, *Adv. Funct. Mater.* **2017**, *27*, 1700526.
 [26] A. Tamayo, S. Riera-Galindo, A. O. F. Jones, R. Resel, M. Mas-Torrent, *Adv. Mater. Interfaces* **2019**, *6*, 1900950.
 [27] S. Riera-Galindo, A. Tamayo, M. Mas-Torrent, *ACS Omega* **2018**, *3*, 2329.
 [28] S. Yun, A. Marrocchi, L. Vaccaro, C. Kim, *Synth. Met.* **2022**, *291*, 117209.
 [29] Y. Xu, C. Liu, D. Khim, Y.-Y. Noh, *Phys. Chem. Chem. Phys.* **2015**, *17*, 26553.
 [30] X. Sun, L. Zhang, C. Di, Y. Wen, Y. Guo, Y. Zhao, G. Yu, Y. Liu, *Adv. Mater.* **2011**, *23*, 3128.
 [31] Z. Lu, C. Wang, W. Deng, M. Tehinke Achille, J. Jie, X. Zhang, *J. Mater. Chem. C* **2020**, *8*, 9133.
 [32] H. F. Haneef, A. M. Zeidell, O. D. Jurchescu, *J. Mater. Chem. C* **2020**, *8*, 759.
 [33] S. Casalini, C. Augusto Bortolotti, F. Leonardi, F. Biscarini, *Chem. Soc. Rev.* **2017**, *46*, 40.
 [34] M. Li, M. Liu, F. Qi, F. R. Lin, A. K.-Y. Jen, *Chem. Rev.* **2024**, *124*, 2138.
 [35] S. Riera-Galindo, L. Chen, M. S. Maglione, Q. Zhang, S. T. Bromley, C. Rovira, M. Mas-Torrent, *Appl. Phys. A* **2022**, *128*, 322.
 [36] A. Campos, S. Riera-Galindo, J. Puigdollers, M. Mas-Torrent, *ACS Appl. Mater. Interfaces* **2018**, *10*, 15952.
 [37] Z. He, J. Chen, D. Li, *Soft Matter* **2019**, *15*, 5790.
 [38] S. Riera-Galindo, F. Leonardi, R. Pfattner, M. Mas-Torrent, *Adv. Mater. Technol.* **2019**, *4*, 1900104.
 [39] T. Salzillo, A. Campos, A. Babuji, R. Santiago, S. T. Bromley, C. Ocal, E. Barrena, R. Jouclas, C. Ruzie, G. Schweicher, Y. H. Geerts, M. Mas-Torrent, *Adv. Funct. Mater.* **2020**, *30*, 2006115.
 [40] K. L. McCall, S. R. Rutter, E. L. Bone, N. D. Forrest, J. S. Bissett, J. D. E. Jones, M. J. Simms, A. J. Page, R. Fisher, B. A. Brown, S. D. Ogier, *Adv. Funct. Mater.* **2014**, *24*, 3067.
 [41] T. Salzillo, F. D’Amico, N. Montes, R. Pfattner, M. Mas-Torrent, *CrytEngComm* **2021**, *23*, 1043.
 [42] J. Li, A. Tamayo, A. Quintana, S. Riera-Galindo, R. Pfattner, Y. Gong, M. Mas-Torrent, *J. Mater. Chem. C* **2023**, *11*, 8178.
 [43] D. Dremann, E. J. Kumar, K. J. Thorley, E. Gutiérrez-Fernández, J. D. Ververs, J. Daniel Bourland, J. E. Anthony, A. R. Srimath Kandada, O. D. Jurchescu, *Mater. Horiz.* **2024**, *11*, 134.
 [44] I. Fratelli, L. Basiricò, A. Ciavatti, Z. A. Lampart, J. E. Anthony, I. Kymissis, B. Fraboni, *Adv. Mater. Technol.* **2023**, *8*, 2200769.
 [45] A. M. Zeidell, T. Ren, D. S. Filston, H. F. Iqbal, E. Holland, J. D. Bourland, J. E. Anthony, O. D. Jurchescu, *Adv. Sci. (Weinh)* **2020**, *7*, 2001522.
 [46] J. A. Posar, M. Petasecca, M. J. Griffith, *Flex. Print. Electron.* **2021**, *6*, 043005.
 [47] S. Lai, P. Cosseddu, L. Basiricò, A. Ciavatti, B. Fraboni, A. Bonfiglio, *Adv. Electron. Mater.* **2017**, *3*, 1600409.
 [48] A. Ciavatti, L. Basiricò, I. Fratelli, S. Lai, P. Cosseddu, A. Bonfiglio, J. E. Anthony, B. Fraboni, *Adv. Funct. Mater.* **2019**, *29*, 1806119.
 [49] K.-J. Baeg, M. Binda, D. Natali, M. Caironi, Y.-Y. Noh, *Adv. Mater.* **2013**, *25*, 4267.
 [50] X. Huang, D. Ji, H. Fuchs, W. Hu, T. Li, *ChemPhotoChem* **2020**, *4*, 9.
 [51] H. Ren, J.-D. Chen, Y.-Q. Li, J.-X. Tang, *Adv. Sci.* **2021**, *8*, 2002418.

- [52] S. Lai, G. Casula, P. Cosseddu, L. Basiricò, A. Ciavatti, F. D'Annunzio, C. Loussert, V. Fischer, B. Fraboni, M. Barbaro, A. Bonfiglio, *Org. Electron.* **2018**, *58*, 263.
- [53] S. G. Surya, H. N. Raval, R. Ahmad, P. Sonar, K. N. Salama, V. R. Rao, *TrAC, Trends Anal. Chem.* **2019**, *111*, 27.
- [54] Y.-C. Lin, W.-C. Yang, Y.-C. Chiang, W.-C. Chen, *Small Sci.* **2022**, *2*, 2100109.
- [55] L. A. DeWerd, L. K. Wagner, *Appl. Radiat. Isot.* **1999**, *50*, 125.
- [56] M. Hoheisel, *Nucl. Instrum. Methods Phys. Res., Sect. A* **2006**, *563*, 215.
- [57] N. Usanase, B. Uzun, D. U. Ozsahin, I. Ozsahin, *Jpn. J. Radiol.* **2024**, *42*, 145.
- [58] L. Basiricò, A. Ciavatti, I. Fratelli, D. Dreossi, G. Tromba, S. Lai, P. Cosseddu, A. Bonfiglio, F. Mariotti, C. Dalla Val, V. Bellucci, J. E. Anthony, B. Fraboni, *Front. Phys.* **2020**, *8*, <https://doi.org/10.3389/fphy.2020.00013>.
- [59] P. Zygmanski, C. Abkai, Z. Han, Y. Shulevich, D. Menichelli, J. Hesser, *J. Appl. Clin. Med. Phys.* **2014**, *15*, 311.
- [60] J. Seco, B. Clasia, M. Partridge, *Phys. Med. Biol.* **2014**, *59*, R303.
- [61] L. Basiricò, A. Ciavatti, T. Cramer, P. Cosseddu, A. Bonfiglio, B. Fraboni, *Nat. Commun.* **2016**, *7*, 13063.
- [62] A. Tamayo, I. Fratelli, A. Ciavatti, C. Martínez-Domingo, P. Branchini, E. Colantoni, S. De Rosa, L. Tortora, A. Contillo, R. Santiago, S. T. Bromley, B. Fraboni, M. Mas-Torrent, L. Basiricò, *Adv. Electron. Mater.* **2022**, *8*, 2200293.
- [63] I. Temiño, L. Basiricò, I. Fratelli, A. Tamayo, A. Ciavatti, M. Mas-Torrent, B. Fraboni, *Nat. Commun.* **2020**, *11*, 2136.
- [64] M. Berteau-Rainville, A. Tamayo, T. Leydecker, A. Pezeshki, I. Salzman, M. Mas-Torrent, E. Orgiu, *Appl. Phys. Lett.* **2021**, *119*, 103301.
- [65] R. Hamilton, J. Smith, S. Ogier, M. Heeney, J. E. Anthony, I. McCulloch, J. Veres, D. D. C. Bradley, T. D. Anthopoulos, *Adv. Mater.* **2009**, *21*, 1166.
- [66] Z. He, D. Li, D. K. Hensley, A. J. Rondinone, J. Chen, *Appl. Phys. Lett.* **2013**, *103*, 113301.
- [67] N. Shin, J. Kang, L. J. Richter, V. M. Prabhu, R. J. Kline, D. A. Fischer, D. M. DeLongchamp, M. F. Toney, S. K. Satija, D. J. Gundlach, B. Purushothaman, J. E. Anthony, D. Y. Yoon, *Adv. Funct. Mater.* **2013**, *23*, 366.
- [68] A. C. Arias, F. Endicott, R. A. Street, *Adv. Mater.* **2006**, *18*, 2900.
- [69] L. Qiu, J. A. Lim, X. Wang, W. H. Lee, M. Hwang, K. Cho, *Adv. Mater.* **2008**, *20*, 1141.
- [70] K. Zhao, O. Wodo, D. Ren, H. U. Khan, M. R. Niazi, H. Hu, M. Abdelsamie, R. Li, E. R. Q. Li, L. Yu, B. Yan, M. M. Payne, J. Smith, J. E. Anthony, T. D. Anthopoulos, S. T. Thoroddsen, B. Ganapathysubramanian, A. Amassian, *Adv. Funct. Mater.* **2016**, *26*, 1737.
- [71] A. Tamayo, T. Salzillo, M. Mas-Torrent, *Adv. Mater. Interfaces* **2022**, *9*, 2101679.
- [72] W. L. Kalb, B. Batlogg, *Phys. Rev. B* **2010**, *81*, 035327.
- [73] S. Kim, H. Yoo, J. Choi, *Sensors* **2023**, *23*, 2265.
- [74] R. Schmechel, H. von Seggern, *Phys. Status Solidi* **2004**, *201*, 1215.
- [75] H. Klauk, *Chem. Soc. Rev.* **2010**, *39*, 2643.
- [76] J. Veres, S. Ogier, G. Lloyd, D. de Leeuw, *Chem. Mater.* **2004**, *16*, 4543.
- [77] H. Bai, Y. Yang, R. M. Voyles, R. A. Nawrocki, *J. Mater. Chem. C* **2022**, *10*, 10973.
- [78] D. Ho, H. Jeong, S. Choi, C. Kim, *J. Mater. Chem. C* **2020**, *8*, 14983.
- [79] Z. He, S. Bi, K. Asare-Yeboah, *Processes* **2024**, *12*, 1944.
- [80] X. Wu, R. Jia, J. Jie, M. Zhang, J. Pan, X. Zhang, X. Zhang, *Adv. Funct. Mater.* **2019**, *29*, 1906653.
- [81] C. Guo, Z. Yang, L. Qin, J. Man, T. Zhang, D.-K. Wang, Z.-H. Lu, Q. Zhu, *J. Mater. Sci.: Mater. Electron.* **2022**, *33*, 3726.
- [82] T. Okachi, *Org. Electron.* **2018**, *57*, 34.
- [83] Z. Yang, C. Guo, C. Shi, D.-K. Wang, T. Zhang, Q. Zhu, Z.-H. Lu, *ACS Appl. Mater. Interfaces* **2020**, *12*, 41886.
- [84] H. F. Iqbal, Q. Ai, K. J. Thorley, H. Chen, I. McCulloch, C. Risko, J. E. Anthony, O. D. Jurchescu, *Nat. Commun.* **2021**, *12*, 2352.
- [85] P. A. Bobbert, A. Sharma, S. G. J. Mathijssen, M. Kemerink, D. M. de Leeuw, *Adv. Mater.* **2012**, *24*, 1146.
- [86] C. Liu, Y. Xu, Y. Li, W. Scheideler, T. Minari, *J. Phys. Chem. C* **2013**, *117*, 12337.
- [87] M. Kunii, H. Iino, J. Hanna, *Appl. Phys. Lett.* **2017**, *110*, 243301.
- [88] S. G. J. Mathijssen, M.-J. Spijkman, A.-M. Andringa, P. A. van Hal, I. McCulloch, M. Kemerink, R. A. J. Janssen, D. M. de Leeuw, *Adv. Mater.* **2010**, *22*, 5105.
- [89] Y. Chen, W. Deng, X. Zhang, M. Wang, J. Jie, *J. Phys. D: Appl. Phys.* **2021**, *55*, 053001.
- [90] H. F. Iqbal, M. Waldrip, H. Chen, I. McCulloch, O. D. Jurchescu, *Adv. Electron. Mater.* **2021**, *7*, 2100393.
- [91] C. G. Tang, K. Hou, W. L. Leong, *Chem. Mater.* **2024**, *36*, 28.
- [92] S. Illig, A. S. Eggeman, A. Troisi, L. Jiang, C. Warwick, M. Nikolka, G. Schweicher, S. G. Yeates, Y. Henri Geerts, J. E. Anthony, H. Sirringhaus, *Nat. Commun.* **2016**, *7*, 10736.
- [93] L. Tortora, M. Urbini, A. Fabbri, P. Branchini, L. Mariucci, M. Rapisarda, M. Barra, F. Chiarella, A. Cassinese, F. Di Capua, A. Aloisio, *Appl. Surf. Sci.* **2018**, *448*, 628.
- [94] J. Li, E. Colantoni, I. Temiño, P. Branchini, L. Tortora, M. Mas-Torrent, *Chem. Mater.* **2023**, *35*, 1527.
- [95] T. Shen, H. Zhou, X. Liu, Y. Fan, D. D. Mishra, Q. Fan, Z. Yang, X. Wang, M. Zhang, J. Li, *ACS Omega* **2020**, *5*, 10891.
- [96] Y. Wang, D. Hu, M. Chen, X. Wang, H. Lu, G. Zhang, X. Wang, Z. Wu, L. Qiu, *Org. Electron.* **2014**, *15*, 3101.
- [97] F. Leonardi, Q. Zhang, Y.-H. Kim, M. Mas-Torrent, *Mater. Sci. Semi-cond. Process.* **2019**, *93*, 105.
- [98] M.-B. Madec, D. Crouch, G. Rincon Llorente, T. J. Whittle, M. Geoghegan, S. G. Yeates, *J. Mater. Chem.* **2008**, *18*, 3230.
- [99] M. R. Niazi, R. Li, E. Qiang Li, A. R. Kirmani, M. Abdelsamie, Q. Wang, W. Pan, M. M. Payne, J. E. Anthony, D.-M. Smilgies, S. T. Thoroddsen, E. P. Giannelis, A. Amassian, *Nat. Commun.* **2015**, *6*, 8598.
- [100] K. Singsumphan, *Mater. Today: Proc.* **2017**, *4*, 6478.
- [101] C. Teixeira da Rocha, K. Haase, Y. Zheng, M. Löffler, M. Hamsch, S. C. B. Mannsfeld, *Adv. Electron. Mater.* **2018**, *4*, 1800141.
- [102] X. Zhao, P. Du, F. Qiu, Y. Hou, H. Lu, J. Zhang, X. Geng, G. Dun, S. Chen, M. Lei, T.-L. Ren, *Adv. Compos. Hybrid Mater.* **2024**, *7*, 192.
- [103] P. S. Jo, D. T. Duong, J. Park, R. Sinclair, A. Salleo, *Chem. Mater.* **2015**, *27*, 3979.
- [104] K. Haase, C. Teixeira da Rocha, C. Hauenstein, Y. Zheng, M. Hamsch, S. C. B. Mannsfeld, *Adv. Electron. Mater.* **2018**, *4*, 1800076.
- [105] Z. He, Z. Zhang, S. Bi, *Mater. Adv.* **2022**, *3*, 1953.
- [106] J. Smith, R. Hamilton, M. Heeney, D. M. de Leeuw, E. Cantatore, J. E. Anthony, I. McCulloch, D. D. C. Bradley, T. D. Anthopoulos, *Appl. Phys. Lett.* **2008**, *93*, 253301.
- [107] N. Onojima, N. Akiyama, Y. Mori, T. Sugai, S. Obata, *Org. Electron.* **2020**, *78*, 105597.
- [108] D. K. Hwang, C. Fuentes-Hernandez, J. D. Berrigan, Y. Fang, J. Kim, W. J. Potscavage, H. Cheun, K. H. Sandhage, B. Kippelen, *J. Mater. Chem.* **2012**, *22*, 5531.
- [109] J.-H. Kwon, S.-I. Shin, K.-H. Kim, M. J. Cho, K. N. Kim, D. H. Choi, B.-K. Ju, *Appl. Phys. Lett.* **2009**, *94*, 013506.
- [110] Z. He, Z. Zhang, S. Bi, J. Chen, *Electron. Mater. Lett.* **2020**, *16*, 441.
- [111] J. Kang, N. Shin, D. Y. Jang, V. M. Prabhu, D. Y. Yoon, *J. Am. Chem. Soc.* **2008**, *130*, 12273.
- [112] D. Bharti, S. P. Tiwari, *Synth. Met.* **2016**, *221*, 186.
- [113] M. McDowell, I. G. Hill, J. E. McDermott, S. L. Bernasek, J. Schwartz, *Appl. Phys. Lett.* **2006**, *88*, 073505.